

# MoSi<sub>2</sub>/Al<sub>2</sub>O<sub>3</sub>/Feldspar Composites for Injection-Molded Ceramic Heating Elements

René Wick-Joliat, Stéphane Mauchle, Roman Kontic, Sandro Ehrat, Thomas Hocker, and Dirk Penner\*

MoSi<sub>2</sub> is an electrically conductive material with numerous applications mostly in high-temperature environments. Herein, the production of MoSi<sub>2</sub>-containing resistive heating elements by ceramic injection molding (CIM) is described. The sintered parts consist of MoSi<sub>2</sub> particles embedded in a matrix of vitrified feldspar and Al<sub>2</sub>O<sub>3</sub>. The conductivity of sintered parts can be tuned precisely by varying the content of the conductive phase. For the development of the injection-molding feedstock, four binder systems are evaluated. The corresponding feedstocks are injection molded into different geometries in traditional molds as well as in additively manufactured, soluble molds. For each feedstock, a debinding and sintering routine is elaborated based on thermogravimetric measurements. Higher debinding temperature leads to more oxidation of MoSi<sub>2</sub> and less conductive samples. Therefore, the conductivity as well as density of sintered parts is used to evaluate the applicability of the feedstocks. Finally, glow tests prove that MoSi<sub>2</sub>/Al<sub>2</sub>O<sub>3</sub>/feldspar composite parts can be used as heating elements and by combining infrared temperature measurement data with computational simulations important material data such as thermal and electrical conductivity and thermal capacity can be obtained reliably.

green parts. In practice, binder systems consisting of a backbone binder (high molecular weight, responsible for structural strength), a lubricant (low molecular weight, ensures good flowability), a surfactant (link between ceramic particles and binder), and a plasticizer (increases plasticity and decrease viscosity) are very common and facilitate the injection-molding process. Debinding and sintering in the end yield ceramic parts with the desired properties.<sup>[2–4]</sup>

MoSi<sub>2</sub> is frequently used in the heating element industry due to its conductivity and excellent stability at high temperatures of up to 1800 °C, which arises from the protective SiO<sub>2</sub> layer forming on the surface of MoSi<sub>2</sub> at temperatures >1000 °C.<sup>[5,6]</sup> At temperatures >1200 °C, MoSi<sub>2</sub> loses creep resistance, which limits its application as a high-temperature structural material. Mechanical properties are largely improved by making composites with a wide range of ceramic reinforcements.<sup>[7–9]</sup>

## 1. Introduction


Ceramic injection molding allows fabrication of complex components with high throughput and high precision.<sup>[1]</sup> The injection molding feedstock is a suspension of a ceramic powder in an organic binder, the latter of which ensures flowability during the injection-molding process and structural integrity of the

Furthermore, its high-temperature stability, together with a high emissivity and potential self-healing properties, makes MoSi<sub>2</sub> attractive as a component in protective shields for spaceflight<sup>[10]</sup> and thermal barrier coatings.<sup>[11,12]</sup> MoSi<sub>2</sub> has also been investigated as a promising cathode for Li–O<sub>2</sub> batteries<sup>[13]</sup> and as a counter electrode for dye-sensitized solar cells (DSSCs).<sup>[14]</sup> Despite being stable at high temperatures, MoSi<sub>2</sub> is well known to undergo pest oxidation at lower temperatures of 400–500 °C, leading to a complete degradation of the material into MoO<sub>3</sub> and SiO<sub>2</sub>.<sup>[5,6,15]</sup> In this study, MoSi<sub>2</sub> particles were protected by embedding them in a glassy matrix. A similar strategy has been used to protect diamonds in grinding wheels from oxidation.<sup>[16]</sup> Therefore, a mixture of MoSi<sub>2</sub> (for conductivity), feldspar (as a glass-forming agent), and Al<sub>2</sub>O<sub>3</sub> was used. The Al<sub>2</sub>O<sub>3</sub> particles improve the mechanical strength of the sintered parts and allow the tuning of the resistivity by adjusting the MoSi<sub>2</sub>/Al<sub>2</sub>O<sub>3</sub> ratio in the composite.<sup>[17,18]</sup> Nevertheless, using this strategy the glass phase only forms during sintering at >800 °C and the debinding conditions have to be tuned carefully to avoid pest oxidation, mainly by keeping the temperature below 400 °C during the debinding step and subsequent sintering in an argon atmosphere.

A commercial binder for ceramic injection molding, Embemould K83, as well as three homemade binder systems

R. Wick-Joliat, S. Mauchle, R. Kontic, D. Penner  
IMPE Institute of Materials and Process Engineering  
ZHAW Zürcher Hochschule für Angewandte Wissenschaften  
Technikumstrasse 9, Winterthur 8401, Switzerland  
E-mail: dirk.penner@zhaw.ch

S. Ehrat, T. Hocker  
ICP Institute of Computational Physics  
ZHAW Zürcher Hochschule für Angewandte Wissenschaften  
Technikumstrasse 9, Winterthur 8401, Switzerland

 The ORCID identification number(s) for the author(s) of this article can be found under <https://doi.org/10.1002/adem.202100517>.

© 2021 The Authors. Advanced Engineering Materials published by Wiley-VCH GmbH. This is an open access article under the terms of the Creative Commons Attribution License, which permits use, distribution and reproduction in any medium, provided the original work is properly cited.

DOI: 10.1002/adem.202100517

consisting of a backbone polymer (high-density polyethylene [HDPE] or low-density polyethylene [LDPE]), an auxiliary binder (paraffin or polyethylene glycol [PEG]), a dispersion medium (stearic acid), and a plasticizer (dibutyl phthalate [DBP]) were investigated in this study. Debinding and sintering conditions were evaluated and optimized and important properties such as conductivity, strength, and density of the injection-molded and sintered parts fabricated with the different binder systems were compared. Bone-shaped MoSi<sub>2</sub> composite parts then underwent glow tests to verify that those parts are suitable heating elements. The electrical and thermal conductivity of the parts were extracted using an infrared camera and computational modeling. In a last step, a recently developed method<sup>[19]</sup> was used to injection mold a range of heating element geometries, such as an M-shaped loop, a spiral, and a helix.

## 2. Experimental Section

### 2.1. General

MoSi<sub>2</sub> powder was purchased from H.C.Starck (Grade A,  $d_{50} = 5.5\text{--}7.5\ \mu\text{m}$ , Figure S1, Supporting Information) and Al<sub>2</sub>O<sub>3</sub> powder was supplied by Almatix (CT19FG,  $d_{50} = 4.0\text{--}7.5\ \mu\text{m}$ , Figure S2, Supporting Information) and feldspar by Sibelco (Spectrum D45, Figure S3, Supporting Information). The other feedstock components used in this study were Embemould K83 (eMBe Products & Service GmbH), HDPE (HD6081, total,  $0.960\ \text{g cm}^{-3}$ ), LDPE (LD 655, ExxonMobil,  $0.913\ \text{g cm}^{-3}$ ), EVA (2048, Schaetti), paraffin ( $T_m$  57–60 °C, Merck), stearic acid (95%, Sigma-Aldrich), and DBP (99%, Sigma-Aldrich). Petroleum ether (boiling point 140 °C) used for solvent debinding was supplied by Carl Roth.

### 2.2. Feedstock Preparation

All feedstocks were prepared using a twin-screw extruder (Thermo Fisher, Process11 Extruder). After extrusion, the feedstock was cooled to  $\approx 50\text{--}70\ ^\circ\text{C}$  and blended using a Nutri Bullet 600 blender. This extrusion and blending cycle was repeated five times. Extrusion temperatures for each feedstock are given in Table 1.

### 2.3. Injection Molding

The resulting fine granules were used for injection molding in a BOY XS machine. Two geometries were molded: rectangular rods 80 mm in length, 10 mm in width, and 4 mm in thickness, and bone-shaped rods with the dimensions of 116 mm in length, 10 mm in width, and 4 mm in thickness and a width of 5 mm in the narrow central part (Figure S4, Supporting Information). The process temperatures used for injection molding are given in Table 1.

The 3D-printed molds used to fabricate more complex geometries were printed using a Prusa SL1 (for the resin frame with though orange resin from Prusa Research) and an Ultimaker 3 (for the polyvinyl alcohol (PVA) mold using PVA supplied by Ultimaker). More details can be found in a separate study on this method.<sup>[19]</sup>

**Table 1.** Composition of the feedstocks used in this study.

Feedstock	Binder composition [wt%]	Solid load	Solid composition [vol%]	Process temperature [°C] <sup>a)</sup>	
Embemould	Embemould K83	100	85 wt%	17 MoSi <sub>2</sub>	130, 140
			68 vol%	27 Al <sub>2</sub> O <sub>3</sub>	
			56	Feldspar	
HDPE/Paraffin	HDPE	45	88 wt%	17 MoSi <sub>2</sub>	170, 190
	Paraffin	46	66 vol%	27 Al <sub>2</sub> O <sub>3</sub>	
	Stearic acid	4	56	Feldspar	
	DBP	5			
LDPE/Paraffin	LDPE	45	88 wt%	17 MoSi <sub>2</sub>	130, 140
	Paraffin	46	65 vol%	27 Al <sub>2</sub> O <sub>3</sub>	
	Stearic acid	4	56	Feldspar	
	DBP	5			
EVA/PEG	EVA	45	84 wt%	17 MoSi <sub>2</sub>	120, 130
	PEG	46	61 vol%	27 Al <sub>2</sub> O <sub>3</sub>	
	Stearic acid	4	56	Feldspar	
	DBP	5			

<sup>a)</sup>First temperature used for feedstock processing, second temperature used for injection molding.

### 2.4. Debinding and Sintering

Green parts molded from Embemould feedstock were pre-debouned in water at room temperature for 24 h and subsequently dried at 40 °C for another 24 h. Green parts with HDPE/paraffin and LDPE/paraffin were debouned in petroleum ether for 24 h at 50 °C and then dried at 40 °C for at least 6 h. Thermogravimetric analysis (TGA) measurements were conducted on a Netzsch 449 C Jupiter instrument. All analyzed specimens were blocks cut from injection-molded rods with a weight of roughly 400 mg and dimensions of roughly 10 × 4 × 4 mm. First, fast scans with a heating rate of 5 K min<sup>-1</sup> up to 600 °C in air atmosphere were conducted to find suitable debinding conditions. Second, debinding and sintering experiments were performed with a heating rate of 1 K min<sup>-1</sup> up to the optimal debinding temperature as determined by the first run, keeping that temperature for 1 h, switching the atmosphere from air to argon and heating to 1250 °C with 5 K min<sup>-1</sup>. This sintering temperature was kept for 2 h before cooling to 30 °C with 8 K min<sup>-1</sup>. The same temperature profiles and process gases were used for debinding/sintering larger samples in a chamber furnace (Carbolite Gero HTK8/KE).

### 2.5. Analysis

The particle size of raw powders MoSi<sub>2</sub>, Al<sub>2</sub>O<sub>3</sub>, and feldspar was measured on a Cilas 1064 particle size analyzer, measuring range 0.04–500.00 μm with 100 steps. Water was used with dispersant Dolapix CE 64. Conductivity of the sintered samples was measured using a multimeter. For this purpose, the ends of the rectangular rods were ground using a Dremel mindrill to remove a non-conductive glass layer on the surface, and subsequently coated with colloidal silver paste. The microstructure and elemental composition of green and sintered parts were assessed

using a Phenom XL Desktop SEM (Thermo Fisher Scientific) equipped with an energy-dispersive X-ray spectroscopy (EDX) analyzer. Densities of sintered parts were measured using the Archimedes method in ethanol.

## 2.6. Glow Tests with IR Camera

Both ends of bone-shaped samples were ground using a Dremel minidrill and galvanized with Cu (acidic  $\text{CuSO}_4$  solution, roughly 20  $\mu\text{m}$ ). An aluminum mesh sleeve was used to assure a tight contact of the Cu layer to the connecting cable of the power supply. A TDK-Lambda Gen300-11 power source was used to control the voltage and monitor the current. The voltage was increased stepwise and IR pictures were recorded after 5 min equilibration time at each voltage step. IR data were recorded using an Optrix Xi400 LTF20 IR camera at a working distance of 400 mm. An emissivity of 0.95 was assumed.

## 2.7. Modeling

Multiphysics software NM-SESES<sup>[20]</sup> was used for modeling by simultaneously solving the differential energy and charge conservation equations in 3D. The latter was used to simulate the distributions of the electrical potential and hence current density from the measured overall heat production. The respective local Joule heating was calculated and used in the heat conduction equation as a source term. This way, the corresponding temperature distribution within the sample was obtained.

The electrical and thermal conductivities as well as the heat capacity were assumed to be temperature-dependent. Note that by assuming a temperature-dependent electrical conductivity a mutual coupling of the electrical and thermal fields is present.

The thermal energy transfer to the surroundings was modeled as boundary conditions assuming thermal radiation in combination with natural convection. For the prior, the Stefan–Boltzmann law was applied with an emissivity value of the sample surface obtained from a sticker with known emissivity. To model natural convection, a temperature-dependent heat transfer coefficient was obtained by applying a Nusselt correlation for horizontal cylinders.

To extract the unknown materials parameters, first, the temperature dependence of the electrical and thermal conductivities was fitted under several steady-state conditions by comparing the simulated and measured surface temperatures and the overall Ohmic resistance of the model with the corresponding experimental value. In a second step, the temperature dependence of the heat capacity was obtained from comparing simulated surface temperatures with the experimental ones for a transient heating process.

## 3. Results and Discussion

The injection molding feedstocks were mixed and homogenized in a twin-screw extruder according to Table 1. The binder content was adjusted to allow good quality injection molding and was 12 wt% for LDPE/paraffin and HDPE/paraffin, 15 wt% for Embemould, and 16 wt% for the EVA/PEG feedstock. Generally, the binder content has to be optimized to match

the rheological requirements for the specific application and the injection molding machine used. The ceramic fraction consisted of 17 vol%  $\text{MoSi}_2$ , 27 vol%  $\text{Al}_2\text{O}_3$ , and 56 vol% feldspar for all feedstocks.

The homogenized feedstocks were blended into granules and used for injection molding. From every feedstock, two different sample geometries were molded: rectangular rods for optimizing debinding and sintering conditions and testing the dimensional stability and “bone-shaped” rods with a narrow central part for glow tests (Figure S4, Supporting Information).

Feedstocks consisting of a backbone binder as well as an auxiliary binder offer the advantage that a solvent pre-debinding can be performed to dissolve the auxiliary binder and make the thermal debinding step faster and prevent defects.<sup>[21]</sup> For EVA/PEG and Embemould feedstocks, water was used to dissolve the auxiliary binder PEG, while paraffin as well as stearic acid and DBP components of the HDPE/paraffin and LDPE/paraffin feedstocks was removed by solvent debinding in petroleum ether.

Suitable thermal debinding conditions were found using TGA. A fast TGA scan with a heating rate of 5  $\text{K min}^{-1}$  gave an estimate on the temperature required to fully remove the binder (Figure 1A). By reducing the heating rate to 1  $\text{K min}^{-1}$ , the samples were fully debound at temperatures 30–40 °C lower than for 5  $\text{K min}^{-1}$  heating rates, a fact that is of utmost importance because  $\text{MoSi}_2$  is prone to pest oxidation at >400 °C. Furthermore, the thermal debinding temperature required for complete debinding typically is 40 °C lower for pre-debound parts as compared to parts without pre-debinding. For example, HDPE/paraffin samples without pre-debinding require 420 °C for full thermal debinding (Figure 1B), whereas only 380 °C is necessary to thermally debind the same feedstock after pre-debinding in water (Figure 1C). In a typical debinding/sintering experiment, the green parts were heated at 1  $\text{K min}^{-1}$  to the temperature that was determined by TGA to be sufficient for complete debinding and that temperature was kept for 1 h before switching to an argon atmosphere and still holding the temperature for another hour. Then, the oven was heated to 1250 °C at 5  $\text{K min}^{-1}$  under the argon atmosphere for sintering and glass formation and held at 1250 °C for 2 h before cooling down at 5  $\text{K min}^{-1}$ .

Figure 1C–F shows a debinding/sintering TGA experiment for each feedstock. The debinding temperatures of 380 °C for HDPE/paraffin and 360 °C for LDPE/paraffin and EVA/PEG were still lower than 400 °C and therefore not in the pest oxidation regime. For the Embemould feedstock, a temperature of at least 400 °C was required to completely remove the binder and the sintered parts showed very low conductivity of <0.1  $\text{S m}^{-1}$ . The conductivity of the Embemould parts could be increased to almost 100  $\text{S m}^{-1}$  using a slower heating rate of only 0.25  $\text{K min}^{-1}$ . In this way, complete removal of the Embemould binder could be achieved at only 340 °C. However, even small temperature deviations of  $\pm 5$  K resulted in insulating of the samples. For the other feedstocks, conductive samples were obtained with heating rates of 1  $\text{K min}^{-1}$ , making the process much faster and more economical.

Figure 2 compares the appearance of green bodies and sintered parts produced from the different feedstocks. All samples show a high dimensional stability and uniform shrinkage depending on the solid load of the feedstock. The bubbles visible

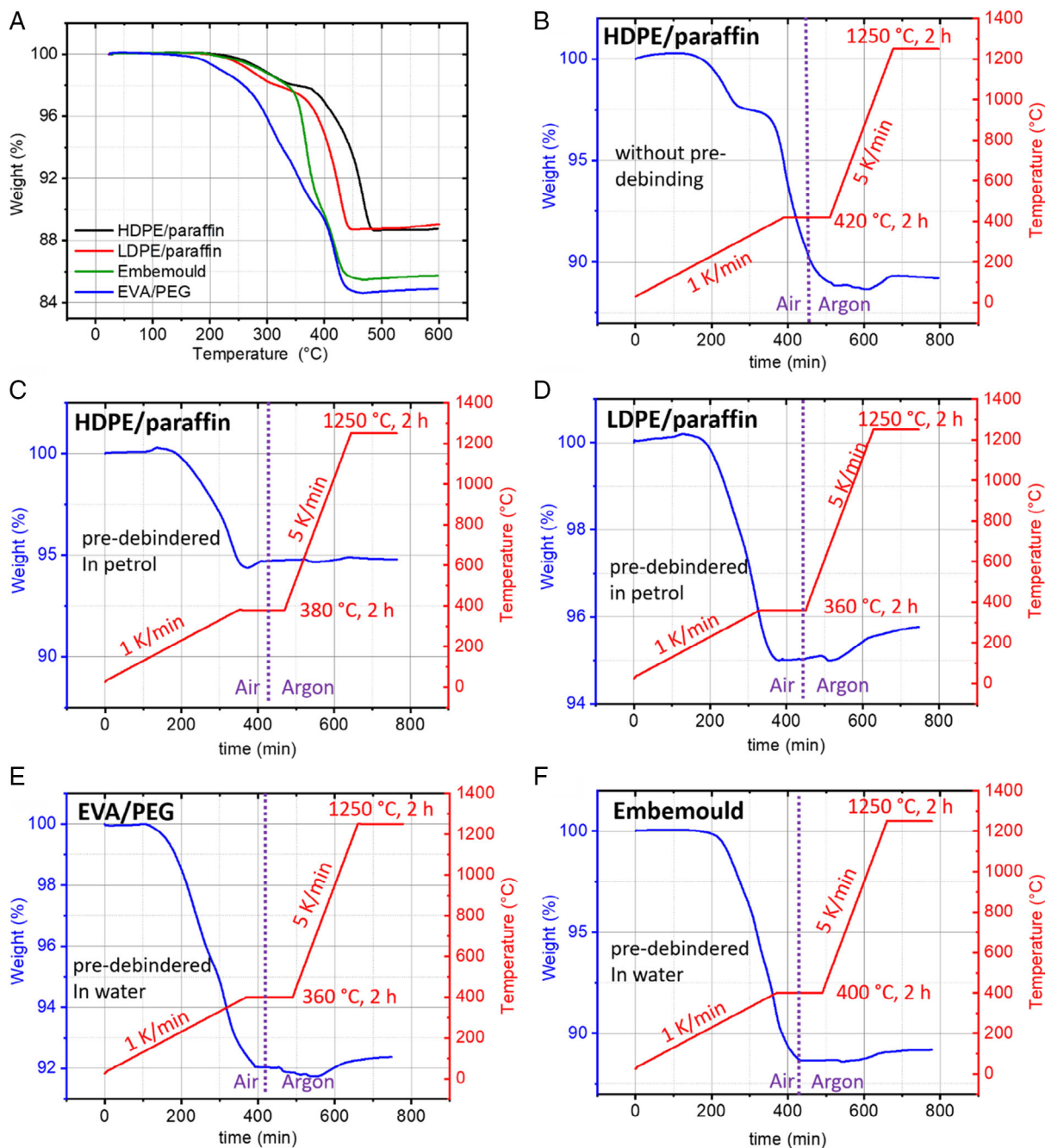


**Figure 1.** A) TGA of feedstocks with various binder systems without pre-debinding; 30–600 °C, heating rate 5 K min<sup>-1</sup>. Weight loss for all samples corresponds nicely to the weight percentage of binder used in the feedstocks according to Table 1, indicating a complete removal of the binder. B) TGA and temperature gradient for HDPE/paraffin feedstock without pre-debinding. TGA and temperature gradient for all feedstocks with pre-debinding in C,D) petrol and E,F) water.

on the LDPE/paraffin samples formed during pre-debinding in petroleum ether and not during sintering. The bubbles are only present on the surface and no pores were found in the bulk of those samples. It is assumed that bubble formation could be avoided by optimizing the pre-debinding conditions using a suitable temperature gradient or petrol with slightly different chemical composition and physical properties.

The conductivity of the sintered samples was measured with the help of a multimeter by grinding the glassy surface at both ends of a rectangular rod and applying colloidal silver paste to the ground ends. The results clearly show that samples molded from feedstocks debound at lower temperatures yield parts with higher conductivity (Figure 3A and Table 2). Highest conductivities were therefore achieved with LDPE/paraffin and EVA/PEG parts



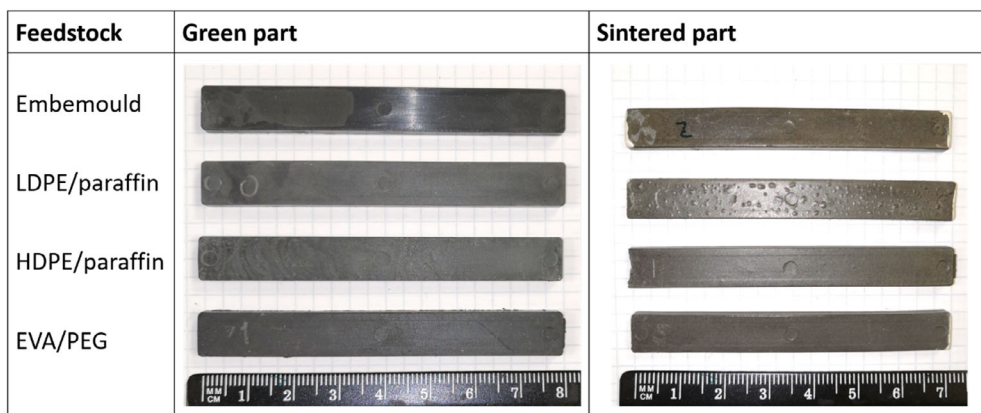


**Figure 2.** Images of injection-molded rods as green bodies and after sintering.

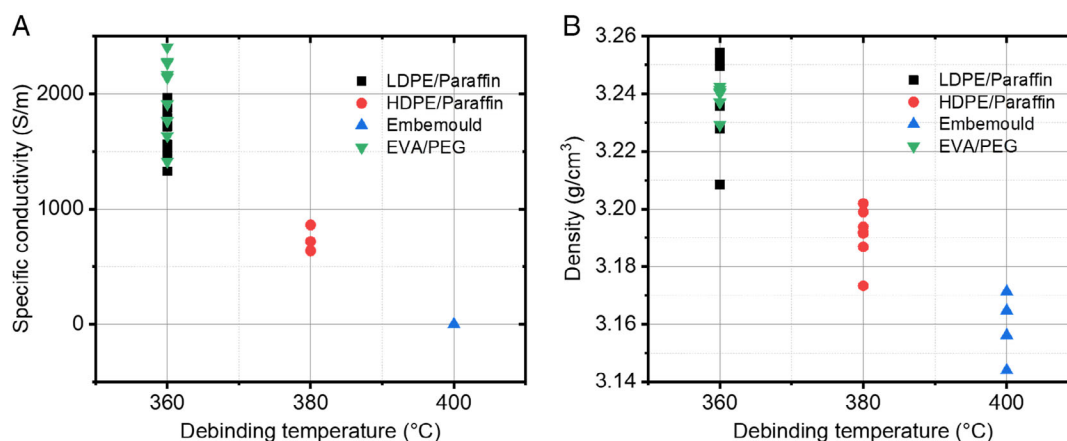


**Figure 3.** A) Specific conductivity versus debinding temperature and B) density versus debinding temperature for individual parts prepared from different feedstocks.

**Table 2.** Conductivity and density of sintered parts prepared from different feedstocks.

Feedstock	MoSi <sub>2</sub> content [vol%]	Thermal debinding temp [°C]	Conductivity [S/m]	Standard deviation [S/m]	Density [g/cm <sup>3</sup> ]	Standard deviation [g/cm <sup>3</sup> ]	Relative density [%]
Embemould	17	400	0		3.159	0.010	88.5
HDPE/paraffin	17	380	744	101	3.191	0.008	89.4
LDPE/paraffin	17	360	1662	186	3.238	0.016	90.7
EVA/PEG	17	360	1985	287	3.238	0.004	90.7

debound at 360 °C, whereas Embemould parts debound at 400 °C showed no conductivity and HDPE/paraffin parts debound at 380 °C gave intermediate conductivity. The same trend was observed when comparing the density of the sintered parts (Figure 3B and Table 2). A lower debinding temperature generally leads to higher density and higher conductivity because MoSi<sub>2</sub> (6.95 g cm<sup>-3</sup>) is partially oxidized to lower density MoO<sub>3</sub> (4.7 g cm<sup>-3</sup>) and SiO<sub>2</sub> (2.2–2.7 g cm<sup>-3</sup>) at temperatures around 400 °C.

By debinding Embemould samples at 360 or 380 °C, their conductivity is increased at the cost of dimensional stability because the parts are not completely debound before sintering and

therefore deformed during the heating to the sintering temperature (Figure 4). The same samples also showed a decreased density when debound at a lower temperature, a trend that is contrary to what we observed in Figure 3B as the low density in this case arises mainly from pore formation and not from oxidation of MoSi<sub>2</sub>.

It should be emphasized that the conductivity of sintered parts can easily be tuned over a wide range by simply increasing or decreasing the MoSi<sub>2</sub> content of the feedstock, depending on the geometry and designated application of the injection-molded parts.

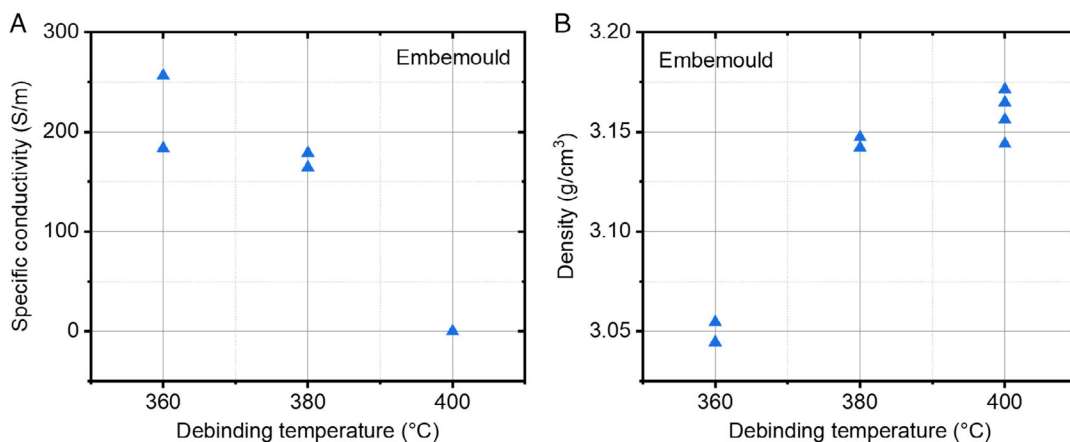


**Figure 4.** A) Specific conductivity versus debinding temperature and B) density versus debinding temperature for individual parts prepared from Embemould feedstocks.

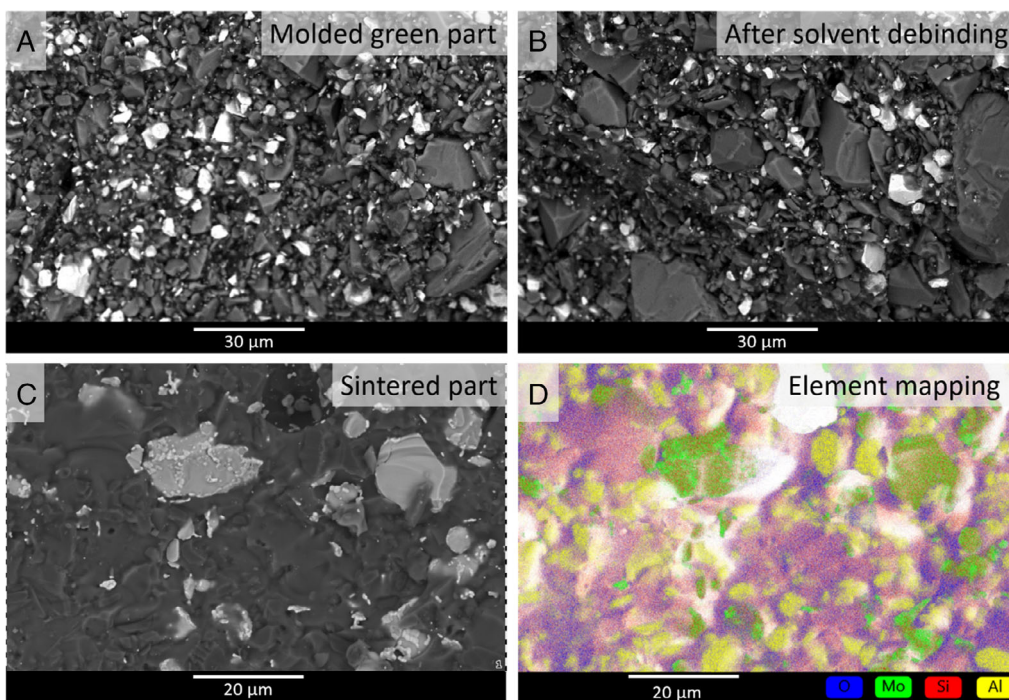


**Figure 5.** SEM images of a green part injection molded from HDPE/paraffin feedstock A) before and B) after solvent debinding. Light gray particles are MoSi<sub>2</sub>, dark gray particles are feldspar and Al<sub>2</sub>O<sub>3</sub>, and black areas correspond to the organic binder. C) After sintering, the MoSi<sub>2</sub> particles are still clearly visible and the feldspar formed a dense glass matrix around MoSi<sub>2</sub> and Al<sub>2</sub>O<sub>3</sub> particles. D) MoSi<sub>2</sub>, Al<sub>2</sub>O<sub>3</sub>, and feldspar can be distinguished by EDX mapping.

Scanning electron microscopy (SEM) and EDX measurements show that the ceramic particles are glued together by the organic binder before debinding (Figure 5A) and to a lesser extent after solvent debinding (Figure 5B). After sintering, the MoSi<sub>2</sub> particles inside the composite are homogeneously embedded in a glass/Al<sub>2</sub>O<sub>3</sub> matrix (Figure 5C,D), which efficiently protects MoSi<sub>2</sub> from oxidation.

To show the potential application of the fabricated parts as heating elements, glow tests were performed and the

experiments monitored by an infrared camera to extract thermal and electrical conductivities of the sintered, bone-shaped parts (Figure 6A). The applied voltage was increased stepwise and the resulting temperature gradient in the sample was measured after a stabilization time of 5 min (Figure 6C). The system was modeled with multiphysics software NM-SESES<sup>[20]</sup> by simultaneously solving the differential energy and charge conservation equations in 3D. Thermal conductivity ( $\kappa$ ) of the samples was calculated to be 12.6 Wm<sup>-1</sup> K<sup>-1</sup> at room temperature, which is

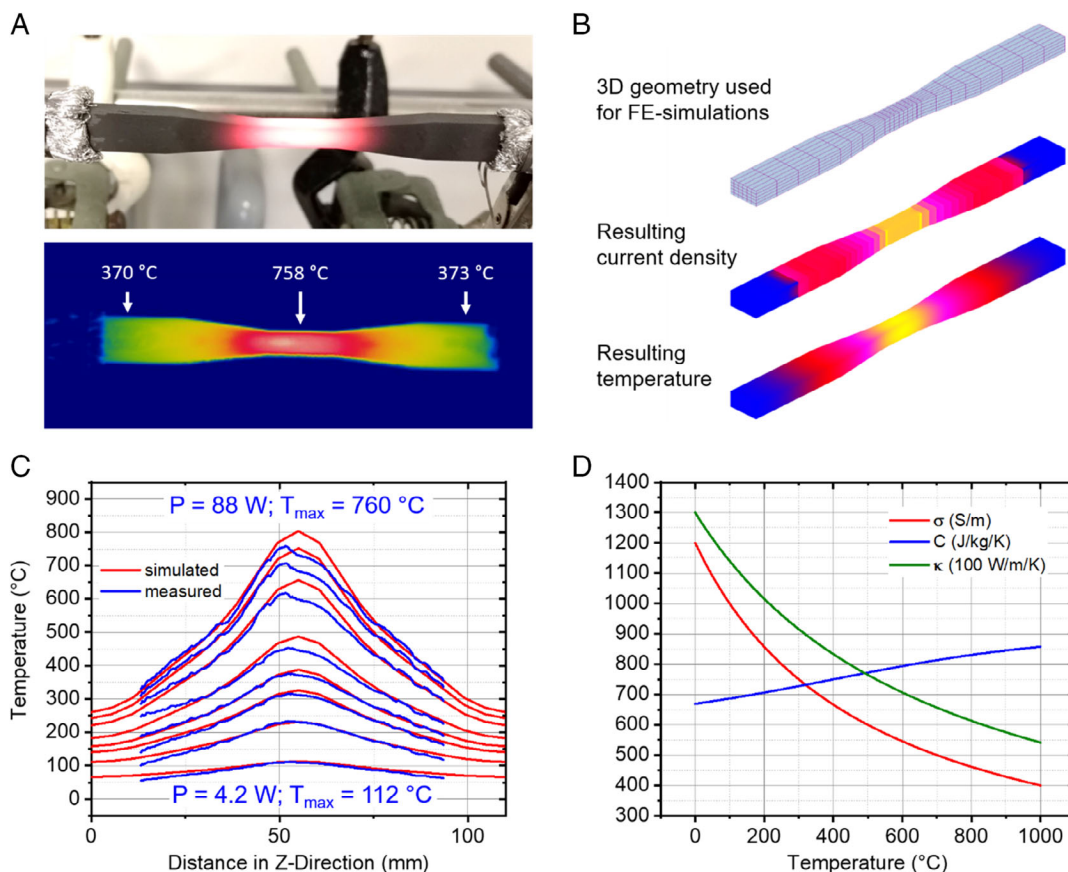


**Figure 6.** A) Photo and infrared picture of a bone-shaped sample fabricated from LDPE/paraffin feedstock at 88 W input power. B) Geometry used for modeling and exemplary simulation results for current density distribution and temperature distribution. C) Temperature gradients measured by infrared camera (blue) and simulated (red) at different input powers ranging from 4.2 to 88 W. D) Material properties extracted from simulations, electrical conductivity  $\sigma$ , thermal conductivity  $\kappa$ , and thermal capacity C.

reasonable given that the material is a composite consisting of  $\text{MoSi}_2$  ( $63 \text{ Wm}^{-1} \text{ K}^{-1}$ ),<sup>[22]</sup>  $\text{Al}_2\text{O}_3$  ( $24 \text{ Wm}^{-1} \text{ K}^{-1}$ ),<sup>[23]</sup> and glass ( $<1 \text{ Wm}^{-1} \text{ K}^{-1}$ ).<sup>[24]</sup> Furthermore,  $\kappa$  decreases with increasing temperature ( $5.4 \text{ Wm}^{-1} \text{ K}^{-1}$  at  $1000 \text{ }^\circ\text{C}$ ) due to the high proportion of  $\text{MoSi}_2$  and  $\text{Al}_2\text{O}_3$  in the samples ( $\text{MoSi}_2$  and  $\text{Al}_2\text{O}_3$  both show a strong  $\kappa$  decrease with increasing  $T$ , whereas for glass  $\kappa$  increases with  $T$ ). Similarly, the electrical conductivity decreases strongly from  $1200 \text{ S m}^{-1}$  at room temperature to  $380 \text{ S m}^{-1}$  at  $1000 \text{ }^\circ\text{C}$ . Therefore, resistance increases by a factor of 2.6 from 25 to  $1000 \text{ }^\circ\text{C}$ , similarly to commercial  $\text{MoSi}_2$  heating elements.

During operation, the resistance of the glowing sample increases slowly due to electromigration and samples fail after 5–14 days of constant operation with direct current.<sup>[25,26]</sup> When alternating current is used, the lifetime is extended drastically. Bone-shaped parts as shown in Figure 7 were tested in alternating current glowing experiments for 28 days. During this time, the resistivity of the samples increased by roughly 10%, mostly within the first 5 days (Figure 7A). This increase in resistivity is attributed to a surface layer of 40–50  $\mu\text{m}$  thickness formed in the hottest part of the glowing sample. Within this layer,  $\text{MoSi}_2$  was transformed into either metallic molybdenum or  $\text{Mo}_5\text{Si}_3$ , whereas no changes in composition or morphology

were found in the bulk of the central part as well as on the surface and in the bulk of the contact area (Figure 7D,E). Detailed studies on the long-term stability, failure mechanisms, and protecting strategies will be extended in the future.

Finally, water-soluble 3D-printed PVA molds were used to fabricate a range of different heating element geometries. This method to produce sacrificial molds for prototyping was developed recently<sup>[19]</sup> and gave good results with the Embemould feedstocks described earlier. However, the  $\text{MoSi}_2$  content was increased to 18 vol% to make the sintered samples more conductive. Figure 8 shows a collection of different heating element geometries as green bodies and under operation in their sintered state.

## 4. Conclusion

Ceramic injection molding feedstocks with four different binder systems were investigated. All feedstocks were suitable for injection molding with the main differences being in their solvent debinding (water for Embemould and EVA/PEG, petroleum ether for HDPE/paraffin and LDPE/paraffin) as well as the temperature needed for the thermal debinding step. Small changes



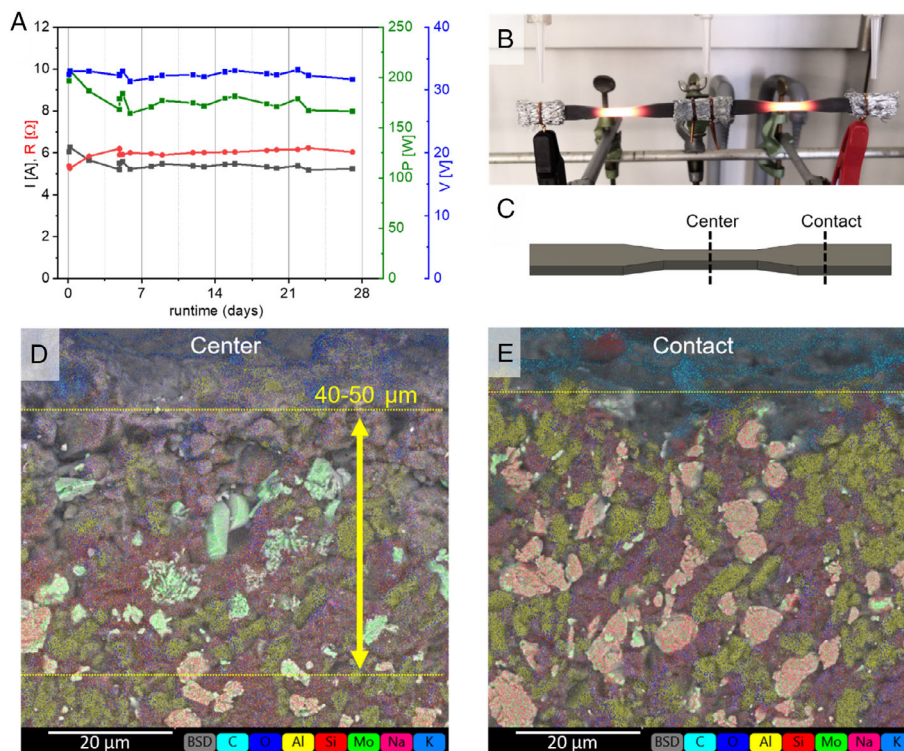


**Figure 7.** Long-term stability measurements on rod-shaped samples fabricated from EVA/PEG feedstock. A) Current  $I$ , resistivity  $R$ , power  $P$ , and Voltage  $V$  versus runtime recorded for 4 weeks. B) Experimental setup with two bone-shaped parts connected in series, because the resistivity of one part alone was too low for the alternating current power supply used. C) Schematic drawing of the part to indicate where the parts were cut for SEM analysis. SEM cross-section image at the surface of the sample after the glow test on the D) central part, showing a layer lacking  $\text{MoSi}_2$ , and E) on the contact area, where no changes are visible after the glow test.

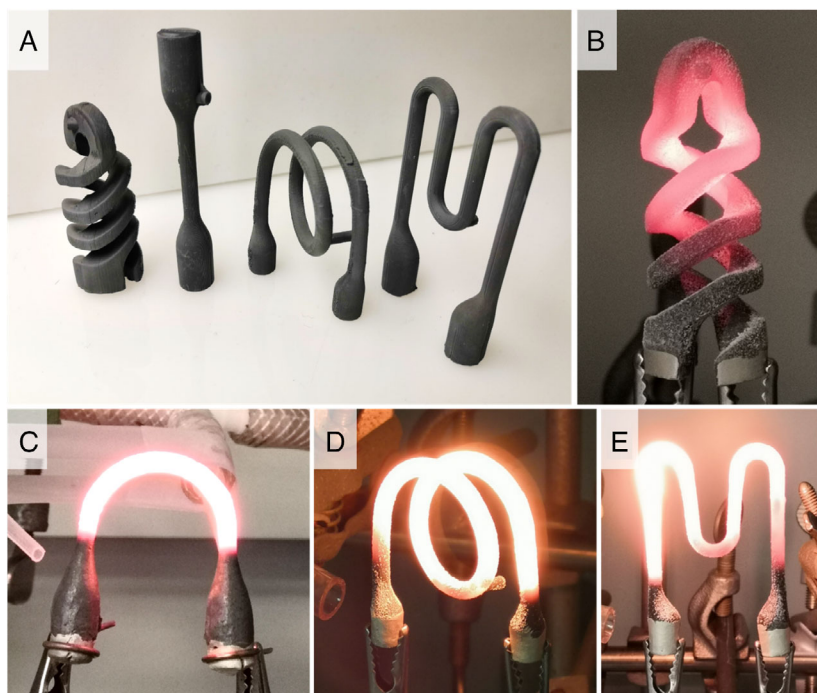


**Figure 8.** A) Photos of green bodies in various geometries injection molded from Embemould feedstock into water-soluble PVA molds and B–E) the sintered parts during glow tests.



in debinding temperature led to a significant difference in the conductivity of the sintered parts due to the partial oxidation of MoSi<sub>2</sub>, which gets more prominent as temperatures approach 400 °C. Therefore, with a fixed MoSi<sub>2</sub> content of 17 vol%, EVA/PEG and LDPE/paraffin feedstocks gave the most conductive samples because they can be fully debound at 340 °C. However, with higher initial MoSi<sub>2</sub> contents, the other feedstocks gave rise to conductive samples as well.

Glow tests on simple bone-shaped samples as well as more complex sample geometries such as spirals and helices showed the applicability of ceramic injection molding for heating element production. Multiphysics modeling allowed us to extract important material parameters such as the temperature-dependent thermal and electrical conductivity as well as heat capacity from IR camera images at different power inputs in glowing heating elements.

## Supporting Information

Supporting Information is available from the Wiley Online Library or from the author.

## Acknowledgements

The authors would like to thank Leister Technologies AG for their cooperation and support and the Swiss Innovation Agency—Innosuisse for funding project 29990.1 IP-ENG.

## Conflict of Interest

The authors declare no conflict of interest.

## Data Availability Statement

Research data are not shared.

## Keywords

binders, ceramic injection molding, heating elements, MoSi<sub>2</sub>

Received: April 29, 2021

Revised: July 22, 2021

Published online: August 16, 2021

- [1] B. C. Mutsuddy, R. G. Ford, *Ceramic Injection Molding*, Chapman & Hall, London **1994**.
- [2] J. Wen, Z. Xie, W. Cao, X. Yang, *J. Adv. Ceram.* **2016**, *5*, 321.
- [3] W. Liu, J. Wen, Z. Xie, X. Yang, *Ceram. Int.* **2018**, *44*, 5646.
- [4] E. Hnatkova, B. Hausnerova, P. Filip, *Ceram. Int.* **2019**, *45*, 20084.
- [5] Y. L. Jeng, E. J. Lavernia, *J. Mater. Sci.* **1994**, *29*, 2557.
- [6] Z. Yao, J. Stiglich, T. S. Sudarshan, *J. Mater. Eng. Perform.* **1999**, *8*, 291.
- [7] Z. Tong, R. He, T. Cheng, K. Zhang, D. Dai, Y. Yang, D. Fang, *Ceram. Int.* **2018**, *44*, 21076.
- [8] J. J. Petrovic, *Mater. Sci. Eng. A* **1995**, *192–193*, 31.
- [9] L. Zhang, Z. Tong, R. He, C. Xie, X. Bai, Y. Yang, D. Fang, *J. Alloys Compd.* **2019**, *780*, 156.
- [10] G. Shao, Y. Lu, X. Wu, J. Wu, S. Cui, J. Jiao, X. Shen, *Appl. Surf. Sci.* **2017**, *416*, 805.
- [11] Z. Derelioglu, A. L. Carabat, G. M. Song, S. van der Zwaag, W. G. Sloof, *J. Eur. Ceram. Soc.* **2015**, *35*, 4507.
- [12] Y. Chen, X. Zhang, S. van der Zwaag, W. G. Sloof, P. Xiao, *J. Am. Ceram. Soc.* **2019**, *102*, 4899.
- [13] C. Dang, Y. Wang, B. He, W. Zhang, F. Dang, H. Wang, Y. Du, *J. Mater. Chem. A* **2020**, *8*, 259.
- [14] M. Wu, Y. Lin, H. Guo, T. Ma, A. Hagfeldt, *J. Power Sources* **2014**, *263*, 154.
- [15] M. Samadzadeh, C. Oprea, H. Karimi Sharif, T. Troczynski, *Int. J. Refract. Met. Hard Mater.* **2017**, *66*, 11.
- [16] K.-H. Lin, S.-F. Peng, S.-T. Lin, *Int. J. Refract. Met. Hard Mater.* **2007**, *25*, 25.
- [17] S. Köbel, J. Plüschke, U. Vogt, T. J. Graule, *Ceram. Int.* **2004**, *30*, 2105.
- [18] X. Fei, Y. Niu, H. Ji, L. Huang, X. Zheng, *Ceram. Int.* **2010**, *36*, 2235.
- [19] R. Wick-Joliat, M. Tschamper, R. Kontic, D. Penner, unpublished **2021**.
- [20] *Multiphysics Software SESES*, n.d. <https://www.zhaw.ch/en/engineering/institutes-centres/icp-institute-of-computational-physics/multiphysics-modeling/multiphysics-software-seses> (accessed: July 2021).
- [21] W.-W. Yang, K.-Y. Yang, M.-C. Wang, M.-H. Hon, *Ceram. Int.* **2003**, *29*, 745.
- [22] S. Bose, R. J. Hecht, *J. Mater. Sci.* **1992**, *27*, 2749.
- [23] J. Hostaša, W. Pabst, J. Matějček, *J. Am. Ceram. Soc.* **2011**, *94*, 4404.
- [24] C. Kittel, *Phys. Rev.* **1949**, *75*, 972.
- [25] D. G. Pierce, P. G. Brusius, *Microelectron. Reliab.* **1997**, *37*, 1053.
- [26] D. Young, A. Christou, *IEEE Trans. Reliab.* **1994**, *43*, 186.